

Impinging jets with fractal grids: heat transfer and flow topology

Stefano Discetti^{1*}, Gioacchino Cafiero², Tommaso Astarita²

¹Aerospace Engineering Group, Universidad Carlos III de Madrid, Leganés, Spain

²Department of Industrial Engineering, Experimental Thermo-Fluid Dynamics Division, Università degli Studi di Napoli Federico II, Naples, Italy

*corresponding author: sdiscett@ing.uc3m.es

Abstract An experimental investigation of the heat transfer and flow features of impinging jets equipped with fractal grids at the nozzle exit is carried out. The heated-thin foil technique is implemented to visualize the spatial distribution of the convective heat transfer rate on the target plate. The heat transfer rate of the impinging jet with a fractal grid is compared to that of a jet without any turbulator under the same condition of power input. In order to understand the complex interaction of wakes of different size with the outer shear layer and with the impinged plate, a fully 3D flow field investigation is carried out with Tomographic particle Image Velocimetry. The results show that a fractal turbulence promoter can provide a significant heat transfer enhancement for relatively small nozzle-to-plate separation. This enhancement can be addressed to the production of streamwise vorticity in the regions of curvature change of the cross-shaped shear layer, generated by the uneven distribution of the blockage ratio.

Keywords: Impinging jets, thermography, PIV, fractals, heat transfer

1 Introduction

The investigation of the flow topology of impinging jets stimulated a flourishing scientific debate in the last 60 years, which is most likely to persist unabated in the next decades. The interest on the topic has been mainly driven by the attractive high-efficiency heat and mass transfer of impinging jets. The high heat/mass transport achieved by fluid jets impinging on surfaces led to countless applications in transversal field of industry, such as cooling of electronic devices [1], glass shaping and tempering [2], food processing [3], turbine blades cooling [4], paper and textile drying [5] and many others. In addition to the variegated portfolio of applications, impinging jets present a set of interesting fundamental phenomenologies (shear-driven instabilities [6,7], vortex-wall interaction [8], self-similar development of the wall jet region [9], etc.).

One of the main paths of investigation concerns with the heat and mass transfer enhancement of impinging jets via passive strategies. Swirling jets [10,11], chevron nozzles [12], tabbed nozzles [13], the use of mesh screens within the nozzle [14] or placed between the nozzle and the target [15], chamfered nozzles [16] or non-circular geometries (lobed [17], elliptic [18]) are some of the solutions adopted in recent times to tamper with the vortical structures and the entrainment rate of impinging jets. In all cases, it has been widely recognized the role of turbulent coherent structures in determining the heat transfer rate. Gardon and Afkirat [19] measured for the first time the profiles of the Nusselt number of an impinging jet and concluded that heat-transfer features cannot be explained only in terms of velocity and local thickness of the wall boundary layer. The turbulence generated by the jet itself due to mixing plays a fundamental role in the heat transfer distribution. In particular, the upstream turbulence has a marked effect in the region close to the stagnation point, which is characterized by strong negative pressure gradients and stably attached flow at the wall. This effect is more significant at short nozzle-plate distances. Kataoka et al [20] addressed the enhanced heat transfer to the presence of large scale coherent structures developing in the jet shear layer due to Kelvin-Helmholtz instability and organized as toroidal vortices. The impingement of these structures for short distance impingement induces pulsating fluctuations of the potential core, thus enhancing its entrainment rate. On the downside, Hadziabdic and Hanjalic [8] observed that the minimum of heat transfer at about 1.5 diameters from the impingement point at nozzle to plate distance between 2 and 4 diameters can be addressed to unsteady flow separation induced by the vortex rings. This effect was already observed on time-averaged heat transfer measurement by Meola et al [21], who addressed the secondary peak of the Nusselt number profile to laminar separation and consequent reattachment of the flow. These works opened the path to strategies to enhance the heat transfer based on promoting turbulence penetration deeper in the jet core. Violato et al [12], for instance, addressed the heat transfer enhancement achieved with chevron nozzles to the

efficient penetration towards the jet axis of the streamwise vortices generated by the chevron. Recently, the authors of the present work [22] proposed to use fractal grids within the nozzle to tune the upstream turbulence level of the incoming jet. A fractal grid is composed of a repeating pattern at increasing small scales. Hurst and Vassilicos [23] outlined that fractal grid generated turbulence with an extended production region, differently from the case of regular grids in which turbulence is built up relatively close to the grid. The position of the maximum turbulent intensity can be tuned simply by scaling the geometrical parameters of the grid [24]. The possibility of tuning the turbulence peak position is an appealing feature of fractal grids towards applications of turbulent mixing enhancement.

In this work, the heat transfer and mean flow field topology of a jet with a fractal insert equal to the one used in [22] and impinging on a plate at small impingement distance is studied.

2 Experimental setup and procedure

2.1 Convective heat transfer measurement setup

A sketch of the experimental setup for convective heat transfer measurement is reported in Figure 1. A heat exchanger conditions in temperature the air supply provided by a fan. A Venturi tube is used to measure the mass flow rate. The air rests in a plenum chamber (where the total pressure is measured); then it passes through a straight pipe of length equal to 6 times the nozzle diameter d (equal to 20mm). A terminating cap of length equal to $1d$ is mounted at the nozzle exits. The grid insert is placed within a small cavity shaped into the cap. The depth of the cavity is 0.5mm , i.e. equal to the grid thickness. In order to minimize the cap influence and to approach the condition of grid placed at the nozzle exit, the cap profile close to the grid location is knife-edged (with angle of 45°). The working fluid impinges normally on a constantan foil of $50\mu\text{m}$ thickness. The plenum chamber is mounted on a precision translation stage to adjust the separation between the nozzle exit section and the target plate (indicated from now on with the symbol z). The constantan foil is heated by Joule effect using a stabilized power supply. The JWT is tested without putting the cap, thus in this case the outflow is that of a straight pipe with length of $6d$.

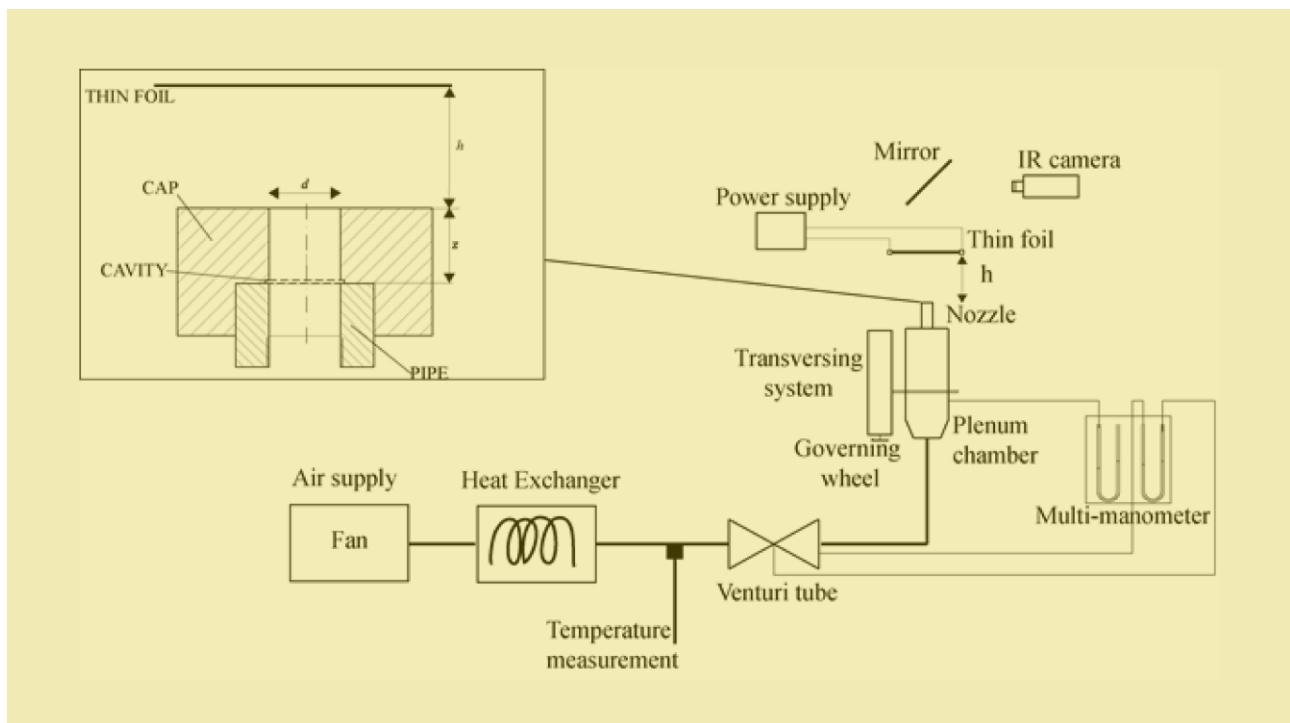


Fig. 1 Sketch of the experimental apparatus for heat transfer measurement (adapted from [22]).

The temperature of the foil is measured from the opposite side to that of impingement using an InfraRed (IR) camera FLIR SC6000 (working in the $8 - 12\mu\text{m}$ band and with 640×512 pixels focal plane array). It can be

assumed that the temperature is uniform across the thickness of the foil since the Biot number ($Bi = h_c s / k_f$, with s being the plate thickness, h_c being the convective heat transfer coefficient and k_f the thermal conductivity of constantan) is very small compared to unity for the entire set of experiments, so the measured temperature is equal to that of the impingement side with good approximation. The imaged side of the plate is covered with a thin layer of high emissivity paint to obtain a satisfactory signal/noise ratio with respect to the surrounding ambient radiation. The achieved resolution of the temperature map is of 3.2 pix/mm , corresponding to 64 pix per diameter.

The temperature maps are averaged over sequences of 1000 statistically independent images and then processed according to the *heated thin foil* sensor model [25]. The distribution of the convective heat flux is presented in terms of the local Nusselt number $Nu = \frac{h_c d}{k}$, with k being the thermal conductivity of the fluid.

The experiments reported here are a set taken from those performed by [22], in which a parametric study on the nozzle-to-plate distance, the grid insert distance from the nozzle exit and the Reynolds number has been performed. In this work only $z/d = 2$ will be considered.

The experiments are carried out at nominal Reynolds numbers equal to 16,000 (using the following expression based on the flow rate, $Re = \frac{4\dot{m}}{\pi\mu d}$).

2.2 Tomographic PIV setup

The experimental setup for the flow field measurement is rendered in Fig.2.

The flow is seeded with olive oil particles (about $1 \mu\text{m}$ diameter), generated by a Laskin nozzle, in order to perform Tomographic PIV experiments. The seeding particles and the working fluid mix in a chamber located upstream of the plenum along the line.

The fluid is illuminated with a Quantel Evergreen Nd:Yag laser with energy of 200mJ/ pulse and beam diameter of about 5mm in the near field.

The Tomo-PIV imaging system is composed of four Andor sCMOS 5.5Mpixels camera equipped with Tokina 100mm macro objectives (set to $f_{\#} = 16$) and Scheimpflug adaptors to achieve proper focusing throughout the imaging region. The cameras are co-planar and subtend a solid angle of about 60° .

An optical calibration is performed by taking images of a target with regularly spaced black dots on white background. The target is moved through the measurement volume using a translational micrometric stage; images are taken at seven different positions along the depth of the measurement volume. A pinhole camera model, modified to take into account effects of optical distortions [26] has been used. The maximum calibration error is of approximately of 0.5pixels. A self-calibration [27,28] procedure, based on the triangulation of the particles position of the images, is carried out in order to shrink this error down to 0.03pixels.

The measurement volume extends for $2.25d \times 1.75d$ in the two directions orthogonal to the nozzle axis (namely X and Z). The depth of the measurement volume is $0.6d$, and it is located right on the impinging plate. The volume is discretized with 41 voxels/mm .

The raw images are pre-processed with the following algorithm: temporal minimum image subtraction; sliding minimum subtraction over a kernel of 7×7 pixels; a sharpening and Gaussian filtering over a 7×7 pixels to smooth the particles shape.

The 3D volume is reconstructed using 5 iterations of the MART algorithm [29], 1 MTE iteration [30] and 3 final MART iterations. A non-isotropic Gaussian smoothing is applied on a $3 \times 3 \times 1$ kernel [31] to reduce the particles elongation along the depth direction. The quality of the reconstruction is checked by computing the signal to noise ratio defined as the reconstructed particles intensity inside the illuminated area versus that reconstructed outside is calculated. The obtained signal to noise ratio is equal to 2, thus providing indication of good quality of the reconstruction.

The reconstructed volume is interrogated using a 3D cross-correlation algorithm. The final interrogation volume of $48 \times 48 \times 48 \text{ voxels}$ ($1.2 \times 1.2 \times 1.2 \text{ mm}^3$), with 75% overlap thus resulting in a vector pitch of 0.3mm. The 3D cross-correlation is performed with the high speed algorithm based on minimization of redundant calculations and sparse matrices developed by [32].

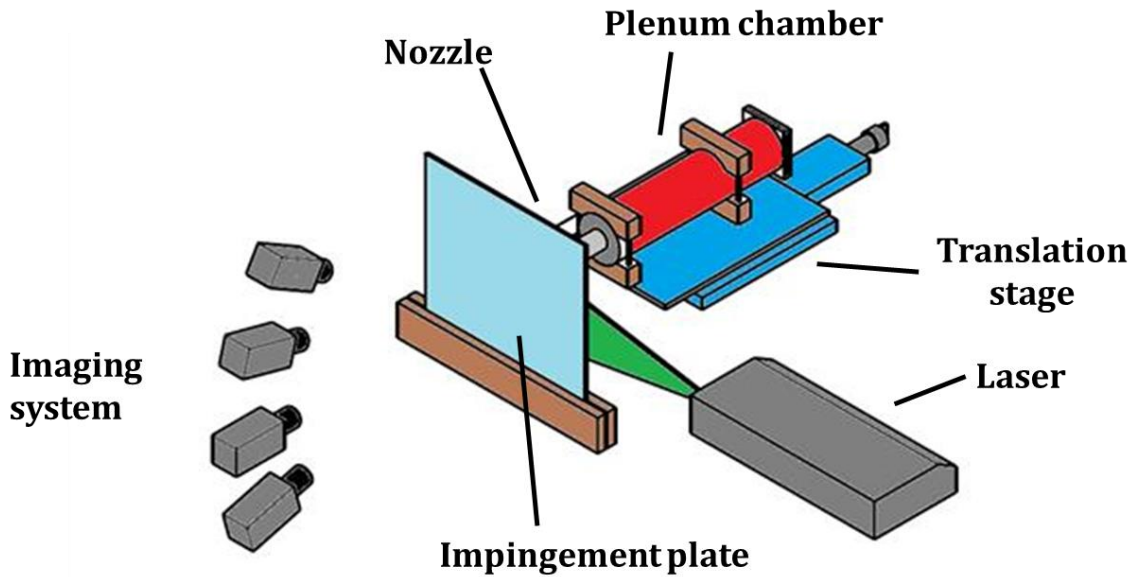


Fig. 2 Sketch of the Tomographic PIV experimental setup.

2.3 Grid inserts

The construction procedure of the fractal grid and the used insert are sketched in Figure 3. The grid is shaped in a 0.5mm thick aluminum foil by laser cutting. The pattern of the fractal grid, repeated at increasingly smaller scales, is a square. The length L_0 and thickness t_0 of the first iteration are respectively equal to 10mm and 1mm. At each iteration length and thickness of the square are both halved. The thickness ratio, i.e. the ratio between the largest and the smallest bar thickness is equal to 4. Using the formula introduced by [23], the grid blockage ratio is equal to 0.32.

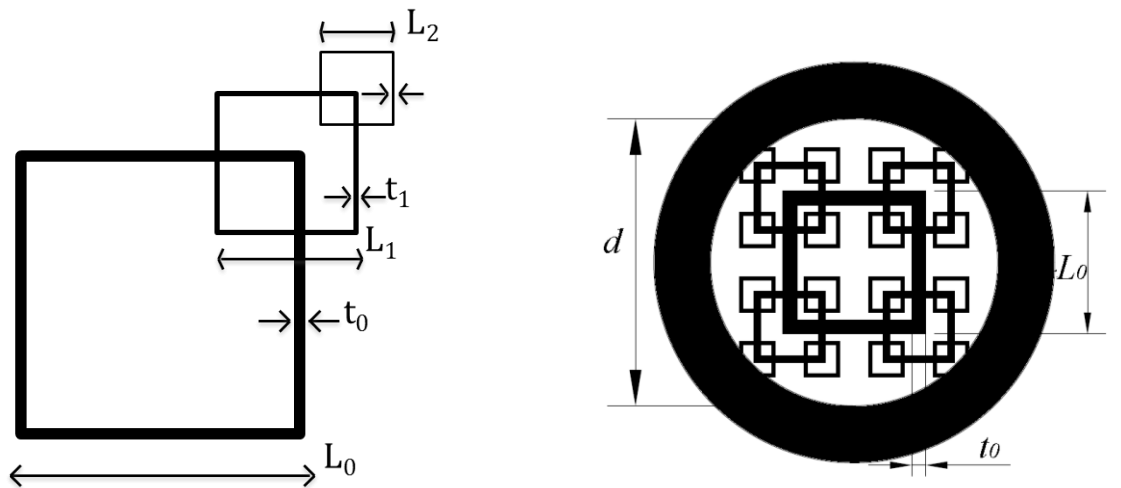


Fig. 3: Fractal grid construction concept (left) and fractal insert (right)

3 Results

In Figure 4 the convective heat transfer coefficient distributions of the impinging jet without the grid (jet without turbulator, JWT) and with the fractal grid (FG) are reported for the analysed case of $Re=16,000$ and $z/d=2$. Evidently the comparison is unfair, since the fractal grid has a larger bulk exit velocity due to the grid

blockage, and consequently it requires a larger power input due to the pressure drop induced by the grid. A more fair comparison, under the same power input conditions, is documented by [27].

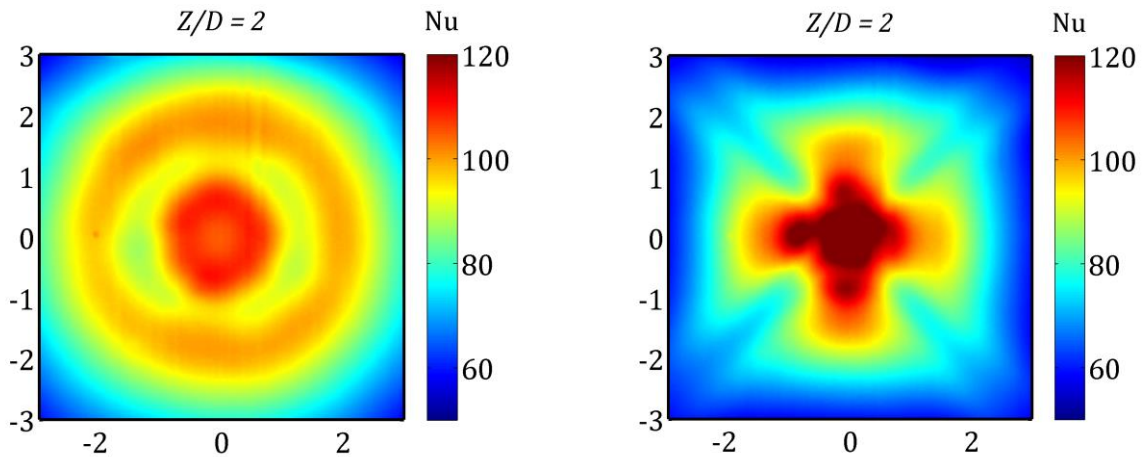


Fig. 4: Nusselt number maps for the jet without turbulence generator (left) and with the fractal grid (right).

The Nusselt number distribution of the circular jet reveals a double-peak shape of the radial profile. Indeed the convective heat transfer flux attains a local minimum at the stagnation point, and then it increases moving away from it. Past a radial distance of approximately 1 diameter, the Nusselt number starts decreasing with the distance, up to a radial distance of $1.5d$. Again, it increases up to a second peak at approximately $2d$ from the stagnation point. This peculiar distribution of the Nusselt number for small nozzle to plate distance is a widely documented phenomenology, on which a debate is still open regarding the cause of its formation. It is commonly accepted that it is addressed to an unsteady separation induced by the impingement of the ring vortices formed by the Kelvin-Helmholtz instability within the jet shear layer.

The Nusselt number distribution for the case of the jet with the fractal grid reveals a local maximum a maximum value of the heat transfer rate at the stagnation point, with much larger intensity than the case of the jet without grid. This is most probably to be ascribed to the larger maximum velocity of the fluid before approaching the stagnation point, generated by the blockage distribution imposed by the grid. The typical cross-pattern of the Nusselt number for the case of the fractal grid can be ascribed to the larger velocity of the fluid arriving from the regions of the grid characterized by smaller blockage, i.e. the central region and the upper/lower/left/right portions of the grid. Along the diagonals of the grid, the secondary iterations determine a larger blockage, thus reducing the flow velocity.

More insightful information can be extracted from flow field measurements. The mean flow field measured with Tomographic PIV is illustrated in Fig.5 together with the Nusselt number distribution on the plate, for the case of jet with and without fractal insert. The slice reporting the velocity magnitude reveals, for the circular jet, the deceleration region along the jet axis when approaching the stagnation point, as well as the region of rotation and acceleration of the fluid which feeds the wall jet which would form for radial distance larger than 3 diameters.

For the case of the jet equipped with fractal grid, as expected the large peak of the Nusselt number in the stagnation region is addressed to the uneven distribution of the mass flow rate, which indeed approaches with larger velocity the jet axis projection on the plate. The contour representation of the velocity on the $y/d = 0$ plane reveals that a strong on-plane outflow is induced in the direction orthogonal to that of maximum heat transfer (i.e. the direction corresponding to the diagonal of the grid). This peculiar feature can be better explained by observing the planes $z/d = 0.1$ and 0.3 reported in Figure 6, in conjunction with the corresponding Nusselt number distribution. At a distance of 0.3 diameters from the impinging plate, the jet presents 5 distinct peaks of velocity, corresponding to the regions of low blockage of the grid. Surprisingly, when approaching the wall, the velocity redistributes so that the strongest wall jets occur along the direction corresponding to the diagonals of the grid, in a fashion that resembles the well-known axis inversion of cross-shaped jets. In this phenomenology the main agent appears to be the curvature change of the shear layer (evident in Figure 6, top right), which is responsible for the formation of streamwise vorticity, as demonstrated by [33] for cross and daisy jets. However, from comparison with Figure 6, bottom, even if interested by larger velocity in the wall jet region, this direction corresponds to that of minimum heat

transfer. This is apparently to be addressed to a non-negligible velocity component in the direction orthogonal to the impingement plate, which reduces the effectiveness of the heat transfer convection of the wall jet.

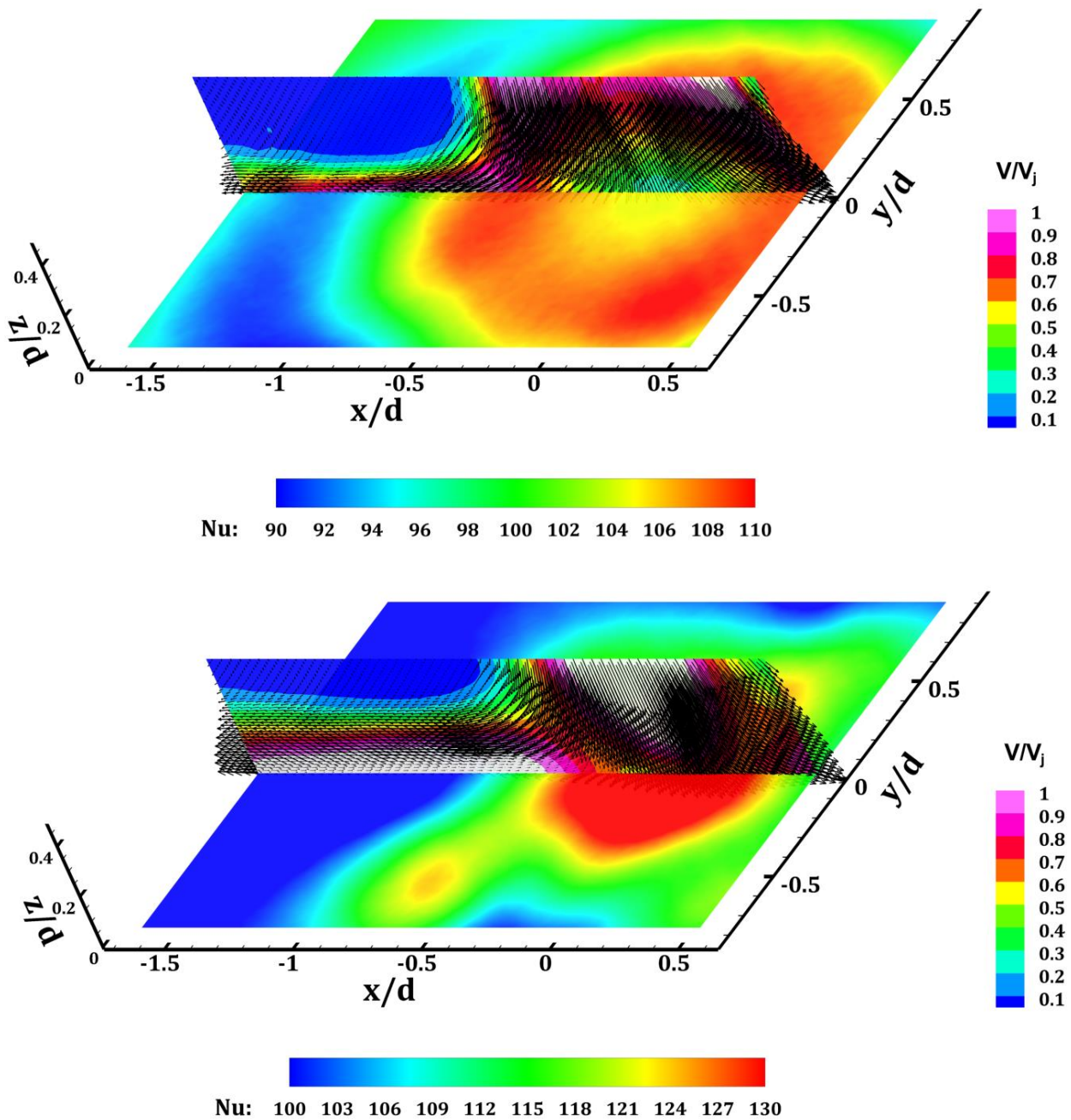


Fig. 5: $y=0$ plane with contour of the magnitude of the velocity and velocity vectors; $z=0$ plane with contour of the Nusselt number. Jet without grid (on top) and with fractal grid (bottom).

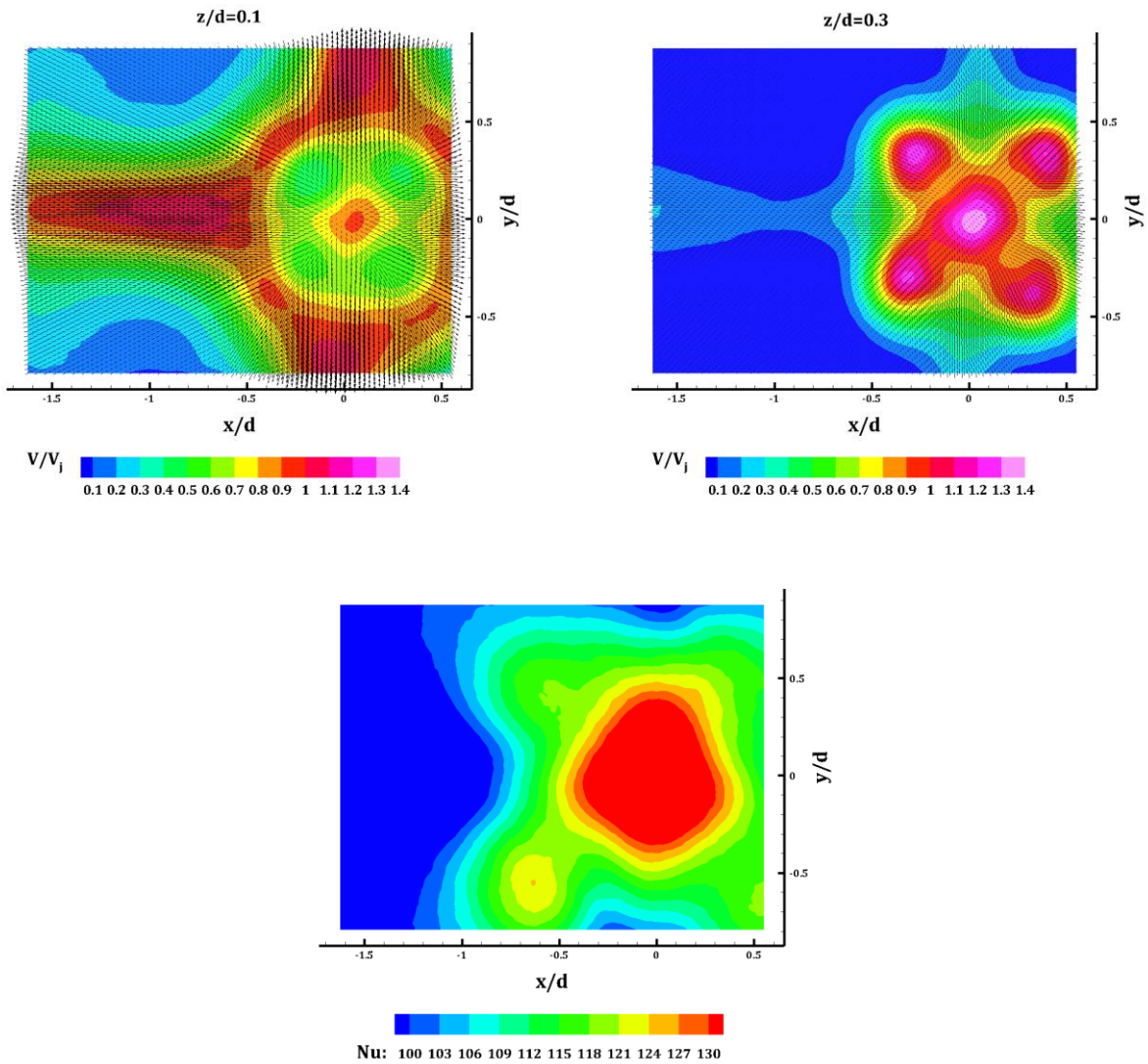


Fig. 6: Top: contour of the velocity magnitude on $z/d=0.1$ (top left) and $z/d=0.3$ (top right) and in-plane velocity vector for the jet equipped with fractal grids. Below, the Nusselt number distribution in the same reference frame for comparison.

4 Conclusions

In this work the heat transfer and flow topology of a circular jet with and without a fractal insert at relatively small impingement distance have been investigated. Particular emphasis is given to the spatial distribution of the heat transfer coefficient and how it correlates with the mean 3D flow features. The circular jet presents the well-known features of the axisymmetric double-peak distribution of the Nusselt number, which has to be addressed to the intermittent effect of the ring vortices developed in the jet shear layer due to the Kelvin-Helmholtz instability, which induce an unsteady separation on the wall. For the case of the jet with fractal grid, the axial symmetry of the heat transfer distribution is suppressed by the reflectional symmetry of the grid. By observing the mean flow field features, the cross-shaped distribution of the heat transfer rate is most likely to be addressed to the impingement velocity distribution, generated by the uneven blockage ratio of the grid. Surprisingly, the fluid flow exhibits an axis inversion as the jet approaches the impingement plate. This is a typical phenomenology of jet with cross-shaped pattern, and it is induced by the curvature of the shear layer, which generates streamwise vorticity. Notwithstanding with this redistribution of the mass flow rate, the region of largest outflow do not correspond to those of maximum heat transfer rate. This aspect will be further investigated by future study, together with possible strategies to improve the heat transfer effectiveness in these regions.

References

- [1] Fabbri M, Dhir V K (2005), Optimized heat transfer for high power electronic cooling using arrays of microjets. *Journal of Heat Transfer*, vol. 127, pp 760-769
- [2] Cirillo F, Isopi G M (2009) Glass tempering heat transfer coefficient evaluation and air jets parameter optimization. *Applied Thermal Engineering* vol. 29, pp 1173-1179.
- [3] Sarkar A, Nitin N, Karwe M V, Singh R P (2004) Fluid flow and heat transfer in air jet impingement in food processing. *Journal of Food Science*, vol.69, CRH113-CRH122
- [4] Hrycak P (1981) Heat transfer from a row of impinging jets to concave cylindrical surfaces-*International Journal of heat and Mass Transfer* vol. 24, pp 407-419.
- [5] Polat S (1993) Heat and mass transfer in impingement drying. *Drying Technology*, vol. 11, pp 1147-1176
- [6] Popiel CO, Trass O (1991) Visualization of a free and impinging round jet. *Experimental Thermal and Fluid Science*, vol. 4, pp 253–264.
- [7] Sakakibara J, Hishida K, Maeda M (1997) Vortex structure and heat transfer in the stagnation region of an impinging plane jet (simultaneous measurements of velocity and temperature fields by digital particle image velocimetry and laser induced fluorescence). *International Journal of Heat and Mass Transfer*, vol. 40, pp 3163–3176.
- [8] Hadziabdic M, Hanjalic K (2008) Vortical structures and heat transfer in a round impinging jet. *Journal of Fluid Mechanics*, vol. 596, pp 221–260.
- [9] Phares D J, Smedley G T, Flagan R C (2000) The wall shear stress produced by the normal impingement of a jet on a flat surface. *Journal of Fluid Mechanics*, vol. 418, pp 315-375.
- [10] Huang L, El-Genk M S (1998) Heat transfer and flow visualization experiments of swirling, multi-channel, and conventional impinging jets. *International Journal of Heat and Mass Transfer*, vol. 41, pp 583–600.
- [11] Ianiro A, Cardone G (2012) Heat transfer rate and uniformity in multichannel swirling impinging jets. *Applied Thermal Engineering*, vol. 49, pp 89–98.
- [12] Violato D, Ianiro A, Cardone G, Scarano F (2012) Three-dimensional vortex dynamics and convective heat transfer in circular and chevron impinging jets. *International Journal of Heat and Fluid Flow*, vol. 37, pp 22–36.
- [13] Gao N, Sun H, Ewing D (2003) Heat transfer to impinging round jets with triangular tabs. *International Journal of Heat and Mass Transfer* 46, 2557–2569 (2003)
- [14] Zhou, D.W., Lee, S.J., “Heat transfer enhancement of impinging jets using mesh screens,” *International Journal of Heat and Mass Transfer*, vol. 47, pp 2097–2108.
- [15] Lee D H, Lee Y M, Kim Y T, Won S Y, Chung Y S (2002) Heat transfer enhancement by the perforated plate installed between an impinging jet and the target plate. *International Journal of Heat and Mass Transfer*, vol. 4, pp 213–217.
- [16] Garimella S V, Nenaydykh B (1996) Nozzle-geometry effects in liquid jet impingement heat transfer. *International Journal of Heat and Mass Transfer*, vol. 39, pp 291–2923.
- [17] Herrero Martin R, Buchlin J M (2011) Jet impingement heat transfer from lobed nozzles. *International Journal of Thermal Sciences*, vol. 50, 1199–1206.
- [18] Lee J, Lee S J (2000) The effect of nozzle configuration on stagnation region heat transfer enhancement of axisymmetric jet impingement. *International Journal of Heat and Mass Transfer*, vol. 43, 3497–3509.
- [19] Gardon R, Afkirat C J (1965) The role of turbulence in determining the heat transfer characteristics of impinging jets. *International Journal of Heat and Mass Transfer*, vol. 8,1261–1272.

- [20] Kataoka K, Suguro M, Degawa H, Maruo K, Mihata I (1987) The effect of surface renewal due to large-scale eddies on jet impingement heat transfer. *International Journal of Heat and Mass Transfer*, vol. 30, pp 559-567.
- [21] Meola C, de Luca L, Carlomagno G M (1996) Influence of shear layer dynamics on impingement heat transfer. *Experimental Thermal and Fluid Science*, vol. 13, pp 29–37.
- [22] Cafiero G, Discetti S, Astarita T (2014) Heat transfer enhancement of impinging jets with fractal-generated turbulence. *International Journal of Heat and Mass Transfer*, vol. 75, pp 173-183.
- [23] Hurst D, Vassilicos J C (2007) Scalings and decay of fractal-generated turbulence. *Physics of Fluids*, vol. 19, 035103.
- [24] Mazellier N, Vassilicos J C (2010) Turbulence without Richardson–Kolmogorov cascade. *Physics of fluids*, vol. 22, 075101.
- [25] Carlomagno G M, Cardone G (2010). Infrared thermography for convective heat transfer measurements. *Experiments in fluids*, vol. 49, pp 1187-1218.
- [26] Tsai R Y (1987). A versatile camera calibration technique for high-accuracy 3D machine vision metrology using off-the-shelf TV cameras and lenses. *IEEE Journal of Robotics and Automation*, vol. 3, pp 323-344.
- [27] Wieneke B (2008). Volume self-calibration for 3D particle image velocimetry. *Experiments in fluids*, vol. 45, pp 549-556.
- [28] Discetti S, Astarita T (2014). The detrimental effect of increasing the number of cameras on self-calibration for tomographic PIV. *Measurement Science and Technology*, vol. 25, 084001.
- [29] Herman G T, Lent A (1976). Iterative reconstruction algorithms. *Computers in biology and medicine*, vol. 6, pp 273-294.
- [30] Novara M, Batenburg K J, Scarano F (2010). Motion tracking-enhanced MART for tomographic PIV. *Measurement Science and Technology*, vol. 21, 035401.
- [31] Discetti S, Natale A, Astarita T (2013). Spatial filtering improved tomographic PIV. *Experiments in fluids*, vol. 54, pp 1-13.
- [32] Discetti S, Astarita T (2012). Fast 3D PIV with direct sparse cross-correlations. *Experiments in fluids*, vol. 53, pp 1437-1451.
- [33] El Hassan M, Meslem A. (2010). Time-resolved stereoscopic particle image velocimetry investigation of the entrainment in the near field of circular and daisy-shaped orifice jets. *Physics of Fluids*, vol. 22, 035107.